Received: 21 January 2021 | Revised: 11 August 2021 | Accepted: 12 August 2021

DOI: 10.1002/hbm.25675

RESEARCH ARTICLE

WILEY

A sub+cortical fMRI-based surface parcellation

John D. Lewis[1] | Gleb Bezgin[1,2] | Vladimir S. Fonov[1] | D. Louis Collins[1] | Alan C. Evans[1]

[1]McConnell Brain Imaging Center, Montreal Neurological Institute, McGill University, Montreal, Quebec, Canada

[2]Translational Neuroimaging Laboratory, The McGill University Research Centre for Studies in Aging, Verdun, Quebec, Canada

Correspondence
John D. Lewis, Montreal Neurological Institute, McGill University, NW147, 3801 University Street, Montreal, QC H3A2B4, Canada.
Email: jlewis@bic.mni.mcgill.ca

Funding information
Azrieli Neurodevelopmental Research Program, Brain Canada Multi-Investigator Research InitiativeAzrieli Foundation, Grant/Award Number: ANRP-MIRI13-3388; Brain Canada Foundation; Canadian Institutes of Health Research; Natural Sciences and Engineering Research Council of Canada; Compute Canada; Calcul Quebec

Abstract

Both cortical and subcortical structures are organized into a large number of distinct areas reflecting functional and cytoarchitectonic differences. Mapping these areas is of fundamental importance to neuroscience. A central obstacle to this task is the inaccuracy associated with bringing results from individuals into a common space. The vast individual differences in morphology pose a serious problem for volumetric registration. Surface-based approaches fare substantially better, but have thus far been used only for cortical parcellation, leaving subcortical parcellation in volumetric space. We extend the surface-based approach to include also the subcortical deep gray-matter structures, thus achieving a uniform representation across both cortex and subcortex, suitable for use with surface-based metrics that span these structures, for example, white/gray contrast. Using data from the Enhanced Nathan Klein Institute—Rockland Sample, limited to individuals between 19 and 69 years of age, we generate a functional parcellation of both the cortical and subcortical surfaces. To assess this extended parcellation, we show that (a) our parcellation provides greater homogeneity of functional connectivity patterns than do arbitrary parcellations matching in the number and size of parcels; (b) our parcels align with known cortical and subcortical architecture; and (c) our extended functional parcellation provides an improved fit to the complexity of life-span (6–85 years) changes in white/gray contrast data compared to arbitrary parcellations matching in the number and size of parcels, supporting its use with surface-based measures. We provide our extended functional parcellation for the use of the neuroimaging community.

KEYWORDS
boundary mapping, cortical parcellation, functional connectivity, model fitting, subcortical parcellation, white/gray contrast

1 | INTRODUCTION

Cortical and subcortical gray matter alike comprise a large number of areas with distinct functional and structural characteristics. A substantial literature is dedicated to how best to identify these areas. Researchers have divided the cortex into regions that are relatively homogenous with respect to cytoarchitecture (Amunts et al., 2005; Brodmann, 1909; Hirai & Jones, 1989; Zilles & Amunts, 2009, 2010); regions based on morphometry (Tzourio-Mazoyer et al., 2002); regions that are relatively homogeneous with

John D. Lewis and Gleb Bezgin contributed equally to this study.

respect to functional connectivity patterns (Gordon et al., 2016; Klein et al., 2007; Wig et al., 2013); and regions that are relatively homogenous across multiple modalities (Glasser, Coalson, et al., 2016). Each of these approaches has advantages and each comes with challenges. One of the most serious challenges, and one that is shared across all parcellation schemes, is the difficulty of mapping the individual results to a common space. Some of these parcellation schemes have relied exclusively on volumetric registration techniques to do this. However, there is a growing appreciation of the limitations of this approach. Individual anatomical variability in brain morphology is problematic, particularly when the age-range of the data is large, or when abnormalities are present. Moreover, additional variability comes with multi-site, multi-protocol data, some of which may include different contrasts for different tissues, for example, blood, which complicates registration. Moreover, to overcome the failings of volume-based registration methods, the data are often blurred before assessing correlation structure; but this blurs data across tissue classes, and will have very different effects in cortical areas with narrow sulci than in cortical areas with wide sulci, or in gray-matter structures of different sizes; and it blurs areal boundaries (Turner & Geyer, 2014; Glasser, Coalson, et al., 2016; Glasser, Smith, et al., 2016; Coalson, Van Essen, & Glasser, 2018). To better deal with the limitations of volume-based registration methods, some recent parcellation methods have turned to surface-based registration approaches for the cortical aspect of this problem, for example, Frost and Goebel (2012), Van Essen, Glasser, Dierker, Harwell, and Coalson (2012), Gordon et al. (2016), and Glasser, Coalson, et al. (2016). Surface-based approaches are significantly more accurate in mapping cortical regions to a common space (Anticevic et al., 2008; Coalson et al., 2018; Fischl et al., 2008; Frost & Goebel, 2012; Glasser, Coalson, et al., 2016; Klein et al., 2010; Lyttelton, Boucher, Robbins, & Evans, 2007; Tucholka, Fritsch, Poline, & Thirion, 2012; Turner & Geyer, 2014). This approach uses the folding pattern instead of voxel intensity to drive a nonlinear surface-based inter-subject registration procedure that aligns the cortical folding patterns of each subject to a standard surface space (Fischl, Sereno, Tootell, & Dale, 1999; Greve & Fischl, 2018). This surface-based approach to the parcellation problem has been taken by a number of researchers, for example, Gordon et al. (2016); Glasser, Coalson, et al. (2016). However, to the best of our knowledge, surface-based parcellation approaches have been restricted to the cortex, with subcortical parcellations remaining at the voxel level. We extend the approach to include the subcortical structures as well as the cortex.

We want a surface-based parcellation for both the cortex and the subcortical structures for two reasons. First, recent research has begun to put surfaces on the subcortical structures, and to derive surface-based metrics from them, for example, white/gray contrast (Lewis et al., 2019). However, many types of analyses rely on parcellations for dimensionality reduction, and currently, there are a variety of cortical parcellations that can be used, but there are no subcortical parcellations. Utilizing arbitrary divisions of the subcortical surface meshes, as done by Lewis et al. (2019) supposes that there is no relation between the metric(s) being examined and the underlying organization, which is highly unlikely, and is likely to combine measures from very different subcortical regions, obscuring both the boundary between them and their individual relationships to other areas.

Second, some of the issues with volumetric registration that a surface-based approach overcomes for the cortex are also issues for registration of the subcortical structures. In part this is because registration of the subcortical structures to a template also involves the cortex; the putamina, for example, are very near to the insular cortex, which is well-known to be morphologically unreliable due to low tissue contrast, and so presents a challenge for tissue segmentation, and also to thin structures like the extreme capsule so volumetric blurring during registration is problematic. The structures that are adjacent to the ventricles present a different but related problem. The ventricles are highly variable, particularly when the population comprises data with a substantial age range, or subjects with disorders. This variability can have a strong negative impact on the registration of adjacent structures, that is, the caudate and thalamus. Likewise, the fornix is extremely variable, and can also negatively impact the registration of the structures near the mid-line. Additionally, the tissue contrast between the deep gray-matter structures and the surrounding white matter is relatively poor compared to that of the cortex and the adjacent white matter, and so also presents a problem for registration. Thus, unsurprisingly, accurate registration of the subcortical deep gray-matter structures is notoriously difficult (Heckemann, Hajnal, Aljabar, Rueckert, & Hammers, 2006). And as with the cortex, the blurring that is used to overcome the failings of volume-based registration methods blurs data across tissue classes, areal boundaries, and even between structures that are separated only by a narrow band of white matter, for example, the globus pallidus and putamen; and for structures that are adjacent to the ventricles, like the thalamus and caudate, such blurring will have an even greater impact. Moreover, inaccurate registration in structures composed of numerous subnuclei will confound parcellation methods. The difficulties associated with volume-based subcortical registration underlie the vast effort that has gone into developing alternate methods. Multiple methods have been proposed to overcome the inadequacies of nonlinear registration, for example, multi-atlas label-fusion. Multi-atlas label-fusion has been shown to fare far better than single-atlas registration for the accurate segmentation of the subcortical structures (Aljabar, Heckemann, Hammers, Hajnal, & Rueckert, 2009; Collins & Pruessner, 2010; Coupé et al., 2011; Heckemann et al., 2006; Lötjönen et al., 2010; Pipitone et al., 2014). This approach uses a library of labeled atlases, and registers either all of, or a subset of, these atlases to a target image. The registered labels are then fused via, for example, patch-based label fusion (Coupé et al., 2011), to produce labels for the target structure. Such an approach provides accurate labels for the subcortical structures, but does not provide a mapping from the segmented subcortical structures to a common space. Lewis et al. (2019) provided a solution to this problem. Lewis et al. (2019) used a multi-atlas label-fusion approach to label the thalamus, caudate, pallidus, and putamen, and then fitted surfaces to these labels, allowing surface registration to provide the mapping from the

segmented subcortical structures to a common space. We draw on those methods to extend surface-based parcellation to include those subcortical deep gray-matter structures, as well as the cortex. Of course, these subcortical surfaces introduce the issue of flattening three-dimensional (3D) structures onto a two-dimensional (2D) manifold. However, if the surface-based measures are determined at the same depth as the functional measures, this will not be a problem. Moreover, of course, a surface parcellation can be constructed at whatever arbitrary depth is desired, or at multiple depths.

Our cortical and subcortical surface-based parcellation approach is an extension of the work of Gordon et al. (2016) who builds on the work of Cohen et al. (2008). Cohen et al. (2008) observed that rs-fMRI connectivity patterns show sharp transitions, which potentially identify areal boundaries. It has since been shown that such transitions correspond to boundaries defined by patterns of cyto- and myeloarchitectonics (Glasser, Coalson, et al., 2016; Gordon et al., 2016; Wig, Laumann, & Petersen, 2014). Gordon et al. (2016) mapped rs-fMRI data to the cortical surface, and built on Cohen et al.'s work to produce all connectivity-based areal boundaries on the cortical surface, and based on these, a cortical parcellation. On the other hand, Gordon et al. (2016) represented the subcortical deep gray-matter structures in volumetric space. We draw on the methods of Lewis et al. (2019) to extend Gordon et al.'s work to include surface-based representations of the subcortical deep gray-matter structures as well as the cortex. We refer to this cortical + subcortical rs-fMRI connectivity-based parcellation as the Bezgin–Lewis extended Gordon (BLeG) parcellation.

Gordon et al. (2016) assessed their parcellation in multiple ways, including in terms of the homogeneity of the functional connectivity patterns within the parcels in comparison to the same for random variants of that parcellation, as well as the fit of their parcellation to the existing data on cytoarchitectonic boundaries. We extend this assessment to the subcortical structures, showing greater within-parcel functional homogeneity in both the cortex and the subcortical structures for BLeG than for random parcellations with the same number of parcels and mean parcel size; and showing that the known architecture of both the cortex and the subcortical structures is reflected in the BLeG parcellation. We further extend the assessment to consider the use of our BLeG parcellation with surface-based metrics, which is our main purpose in proposing this cortical + subcortical parcellation; here we use the white/gray contrast measure of Lewis et al. (2018) and Lewis et al. (2019). This measure is a ratio of the intensities in the white matter and the adjacent gray matter, similar to the measure formulated by Salat et al. (2009). Thus it, in part, reflects the integrity of the white matter adjacent to the gray matter, and, in part, the cellular complexity of the gray matter and the degree of myelination within it, including from invading myelinated fibers. In addition, critically, this measure can be produced for cortex and all subcortical structures; subcortical gray-matter intensity was measured at the same depth as was functional connectivity, thus eliminating the issue of mapping a 3D structure to a 2D manifold. By drawing on the fact that white/gray contrast in different brain regions shows differential relations to age, sex, brain volume, and so forth, which is true for a variety of morphometric measures (Allen, Bruss, Brown, & Damasio, 2005; Goldstein et al., 2001; Kennedy et al., 2009; Raz et al., 1997, 2005; Raz & Rodrigue, 2006; Sowell et al., 2006; Storsve et al., 2014), and particularly for subcortical structures (Goddings et al., 2014; Østby et al., 2009), we devise an assessment of within-parcel model-complexity homogeneity. Here, the linear model that provided the best fit to the white/gray contrast measures at each vertex was determined for life-span data, as well as the complexity of that model, that is, the number of terms in the best-fit model for the data, counting composite terms as more than a single term, but less than the number of base terms it comprises (Section 2.3.4); the homogeneity of model complexity was then computed for every parcel of our extended functional parcellation, BLeG, and the mean of this parcel-wise homogeneity of model complexity provided a measure of how well the overall parcellation aligned with the white/gray contrast data over the life-span. This test was repeated for parcellations based on arbitrary divisions of the surface meshes matching the number and size of parcels. We show that our extended functional parcellation, BLeG, provides an improved fit to the complexity of the life-span changes in the white/gray contrast data compared to these random parcellations, thus indicating the utility of our BLeG parcellation for use with surface-based morphometric data.

2 | MATERIALS AND METHODS

2.1 | Data

The data used here were from the publicly available Enhanced Nathan–Klein Institute—Rockland Sample (Nooner et al., 2012)—commonly known as the NKI-RS data. Data collection received ethics approval through both the Nathan–Klein Institute and Montclair State University. Written informed consent was obtained from all participants, and in the case of minors, also from their legal guardians. All imaging data were acquired from the same scanner (Siemens Magnetom TrioTim, 3.0 T). T1-weighted images were acquired with an MPRAGE sequence (TR = 1,900 ms; TE = 2.52 ms; voxel size = 1 mm isotropic). Resting-state fMRI data were acquired in multiple ways for each subject, varying in temporal and spatial resolution. We utilized the high spatial resolution multiplexed data (TR = 1,400 ms; TE = 30 ms; voxel size = 2 mm isotropic) for the principal parcellation; and the low temporal and spatial resolution data (TR = 2,500; TE = 30 ms; voxel size = 3 mm isotropic) for comparison with Gordon et al.'s (2016) original parcellation. We included all subjects for which there were both usable T1-weighted data and fMRI data. There were 568 such individuals, ranging from 6 to 85 years of age. The BLeG parcellation was constructed from the individuals between 19 and 69 years of age, of which there were 393 (69% of these were female); the data from individuals less than 19 years of age and individuals greater than 70 years of age were used to verify the use of the BLeG parcellation with data from children, adolescents,

and the elderly, as well as the adult data from which it was constructed. There were 115 individuals <19 years of age (48% female), and 60 individuals greater than 70 years of age (68% female).

2.2 | Data processing

The T1-weighted volumes were processed to derive surfaces onto which the fMRI data could be loaded, and from which surface-based measures of white/gray contrast could be computed. These various surfaces are derived from the surfaces that lie at the gray–white boundary and, in the case of the cortex, the gray–CSF boundary; the processing that produces these surfaces is described next. The derivation of the surfaces onto which the fMRI is loaded is described in Section 2.2.1 together with a description of the fMRI processing. The derivation of the surfaces from which the measures of white/gray contrast are computed is described in Section 2.3.4 together with a description of how those measures are computed.

2.2.1 | Surface extraction

The T1-weighted volumes were denoised (Manjón, Coupé, Martí-Bonmatí, Collins, & Robles, 2010) and then processed with CIVET (version 2.1; 2016), a fully automated structural image analysis pipeline developed at the Montreal Neurological Institute.[1] CIVET corrects intensity non-uniformities using N3 (Sled, Zijdenbos, & Evans, 1998); aligns the input volumes to the Talairach-like ICBM-152-nl template (Collins, Neelin, Peters, & Evans, 1994); classifies the image into white matter, gray matter, cerebrospinal fluid, and background (Tohka, Zijdenbos, & Evans, 2004; Zijdenbos, Forghani, & Evans, 2002); extracts the white-matter and pial surfaces (Kim et al., 2005); and maps these to a common surface template (Lyttelton et al., 2007).

Subcortical segmentation into left and right caudate, putamen, globus pallidus, and thalamus was done using a label-fusion-based labeling technique based on Coupé et al. (2011) and further developed by Weier, Fonov, Lavoie, Doyon, and Collins (2014) and by Lewis et al. (2019). The approach uses a population-specific template library. The library was constructed by clustering (as described in Lewis et al., 2019) the deformation fields from the nonlinear transforms produced by CIVET, and using the central-most subject of each cluster to construct the entries in the template library. The number of clusters was specified as the square of the natural log of the number of subjects. To create the library entry for a cluster, the nonlinear transform for the central-most subject was inverted and used to warp the ICBM-152-nl template together with the subcortical segmentation defined on it; this pair was then added to the template library. The template library is thus a set of warped copies of the ICBM-152-nl template together with their correspondingly warped segmentations, and represents the range of deformations found in the population. Once the template library had been created, each subject in the population was nonlinearly registered to the n closest templates in the library (here, $n = 7$), and the resulting transforms were used to warp their corresponding segmentations to the subject; the final labeling was then established via patch-based label fusion.

Once the subcortical structures for a subject were labeled, surfaces defined on the ICBM-152-nl template were fitted to those labels. These model surfaces were warped to each individual based on the transforms derived from the label-fusion-based labeling stage, and then adjusted to the final labels by moving vertices along a distance map created for each label. The surfaces for each structure were then registered to their corresponding common surface template to ensure cross-subject vertex correspondence, as per the cortical surfaces.

Based on these surfaces at the gray–white boundary and, for the cortex, the pial surface, several additional surfaces were created to allow for the surface-based fMRI analysis. The fMRI data were preprocessed (as described in Section 2.2.2) and then loaded onto the cortical midsurface, a surface falling halfway between the surface at the cortical gray–white boundary and the pial surface, and onto surfaces 2 mm inside of the surfaces at the gray–white boundary of the subcortical structures. These choices avoid partial volume effects, to the extent possible. These surfaces are shown in Figure 1.

To create the surfaces 2 mm inside of the surfaces at the gray–white boundary of the subcortical structures, a distance map was created from those surfaces, smoothed with a Gaussian kernel, and used to create a gradient vector field. The subcortical white surfaces were then moved 2 mm along this vector field into the subcortical gray

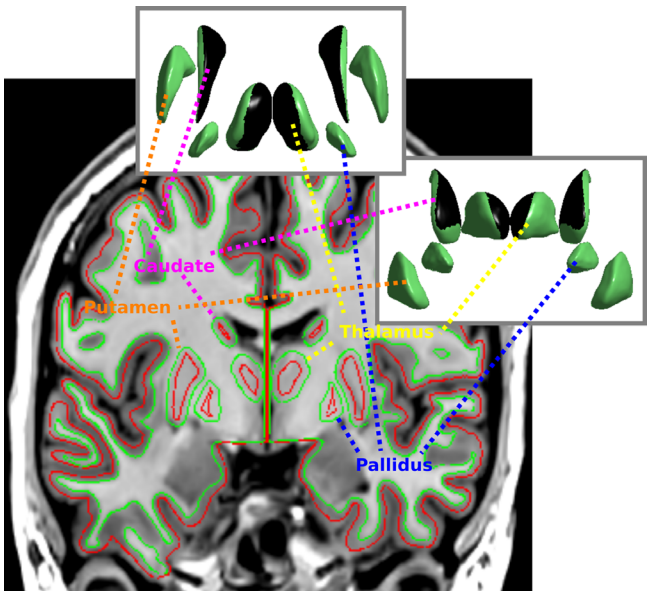

FIGURE 1 An example of the surfaces that the preprocessed fMRI time-series data are projected onto. The coronal slice shows the cortical midsurface in red, as well as the supra-white surfaces within the subcortical gray matter; the fMRI data are projected onto these surfaces. For reference, the surfaces at the gray–white boundary are shown in green. The insets show the top and front views of the subcortical surfaces, with the areas of the thalamus and caudate that are adjacent to the ventricles shown in black. Note that the spatial aspect of the subcortical structures in the insets has been manipulated to provide a view of each structure

matter to produce the subcortical supra-white surfaces. The procedure is described in detail in Lewis et al. (2019).

2.2.2 | rs-fMRI processing

The rs-fMRI data were minimally preprocessed before loading the data onto the surfaces. The approach is essentially that used in *fMRIPrep* (Esteban et al., 2019), adapted to work with CIVET. First, a slice-timing correction was applied with FSL's *slicetimer* (Smith et al., 2004), with the timings for each slice in the multi-band acquisition provided. FSL's motion correction algorithm, *mcflirt* (Jenkinson, Bannister, Brady, & Smith, 2002) was then used to register all volumes to a reference functional volume; the seventh volume was used; the first six volumes were discarded. As well as producing the motion-corrected fMRI data, this procedure provided the motion-correction parameters, and identified motion-contaminated volumes by frame-by-frame displacement (Power, Barnes, Snyder, Schlaggar, & Petersen, 2012). *ICA-AROMA* was then applied to the motion-corrected data to identify independent components associated with motion artifacts, and to remove them from the data (Pruim et al., 2015). Pruim et al. (2015) note, however, that the default settings are not appropriate for use with fast TR data, since important information is available in higher frequencies, which are better resolved in the measured observations of fast TR data, and thus classifying ICs with high-frequency content as motion ICs removes signal from the data (Mayer et al., 2019). Thus we altered the default settings to classify independent components as motion artifacts if and only if they correlated with the realignment parameters from *mcflirt* at a greater than chance level. The fMRI images were then corrected for the distortions associated with echo-planar imaging using large deformation diffeomorphic metric mapping (Miller, Beg, Ceritoglu, & Stark, 2005) based on the T1-weighted volume, with the deformation restricted to the phase encoding direction of the fMRI acquisition. The surfaces described above were then transformed to overlay the distortion-corrected rs-fMRI, and the rs-fMRI data were loaded onto them, that is, the voxel intensities were sampled onto the vertices of the cortical midsurfaces and the subcortical supra-white surfaces.

The connectivity-based parcellation of the rs-fMRI is based on the methods described in Gordon et al. (2016), which builds on the work of Cohen et al. (2008). Cohen et al. (2008) observed that rs-fMRI connectivity patterns show sharp transitions, which potentially identify areal boundaries. Gordon et al. (2016) extended Cohen et al.'s work to produce all cortical connectivity-based areal boundaries, and based on these, a parcellation of the cortex. We further extend this work by including surfaces for the caudate, globus pallidus, putamen, and thalamus, in addition to those for the cortex, producing a parcellation for all of these surfaces. To achieve this, we adapt the code provided by Gordon et al. (2016).[2] We convert the cortical midsurfaces and subcortical supra-white surfaces, with their associated rs-fMRI time courses, to CIFTI,[3] and as per Gordon et al. (2016), for each subject, correlate the time course of each surface vertex (both cortical and subcortical) with that from every other surface vertex. The resultant correlation maps are then transformed using Fisher's *r*-to-*z* transformation. The pairwise correlations between entries in each subject's correlation map comprise that subject's similarity matrix. A set of gradient maps that identify positions of abrupt changes in connectivity patterns are then generated by taking the first spatial derivative in each subject's similarity matrix. The gradient maps are then averaged across subjects, and the average gradient maps are subjected to Beucher's (1979) "watershed by flooding" algorithm to identify potential areal boundaries. The resulting boundary maps are then averaged to yield a map of the frequency with which each vertex is identified as a potential boundary vertex. The resulting boundary map for the high-resolution NKI-RS data is shown in Figure 2; the results for the low-resolution NKI-RS data are provided in Figure S7.

The local minima in the boundary map are seeds for parcel creation. Parcels are expanded outward from these seeds until they either meet another parcel or reach a height threshold on the boundary map. Adjacent parcels are then merged, if they are too similar. Additionally, parcels containing fewer than 30 cortical vertices are merged with the adjacent parcel with the lowest boundary map values separating the two. Finally, vertices with high boundary map values (defined as the top quartile of values in the boundary map) were eliminated from parcels, and treated as transition zones between parcels. This procedure is as implemented by Gordon et al. (2016), and uses the default parameters in that code, with the exception of the boundary threshold in the *parcel_creator* function, which was lowered to 0.5 due to signal loss from ICA-AROMA. The final parcellation is shown in Figure 3. Note that the regions of the subcortical material that are adjacent to the ventricles are masked. This is for two reasons: first, because this parcellation is meant for use with white/gray contrast measures, and white/gray contrast cannot be assessed in these regions; and second, because the signal from fMRI is known to suffer from pulsatory artifacts in areas adjacent to the ventricles (Edelman et al., 1994; Hu, Le, Parrish, & Erhard, 1995; Kim, 1995). Nonetheless, we show the version of the parcellation without these areas masked in Figure S1, and provide it in the release; but people should be wary of those parcels.

2.3 | Assessing the parcellation

Gordon et al. (2016) assessed their parcellation in multiple ways: in terms of the within-parcel homogeneity of functional connectivity patterns; by visually comparing parcel alignment with known cytoarchitectonic areas; and by assessing the stability of the boundary maps across two datasets. We extend these assessments to include the subcortical structures. We assess the within-parcel homogeneity of functional connectivity patterns within both the cortex and the subcortical structures; we compare the placement of the parcels to the known architecture of both the cortex and the subcortical structures; and we assess the stability of the boundary map across developmental data, adult data, and data from elderly individuals. Furthermore, to assess the usefulness of our parcellation with structural metrics, which is the main objective of producing this cortical

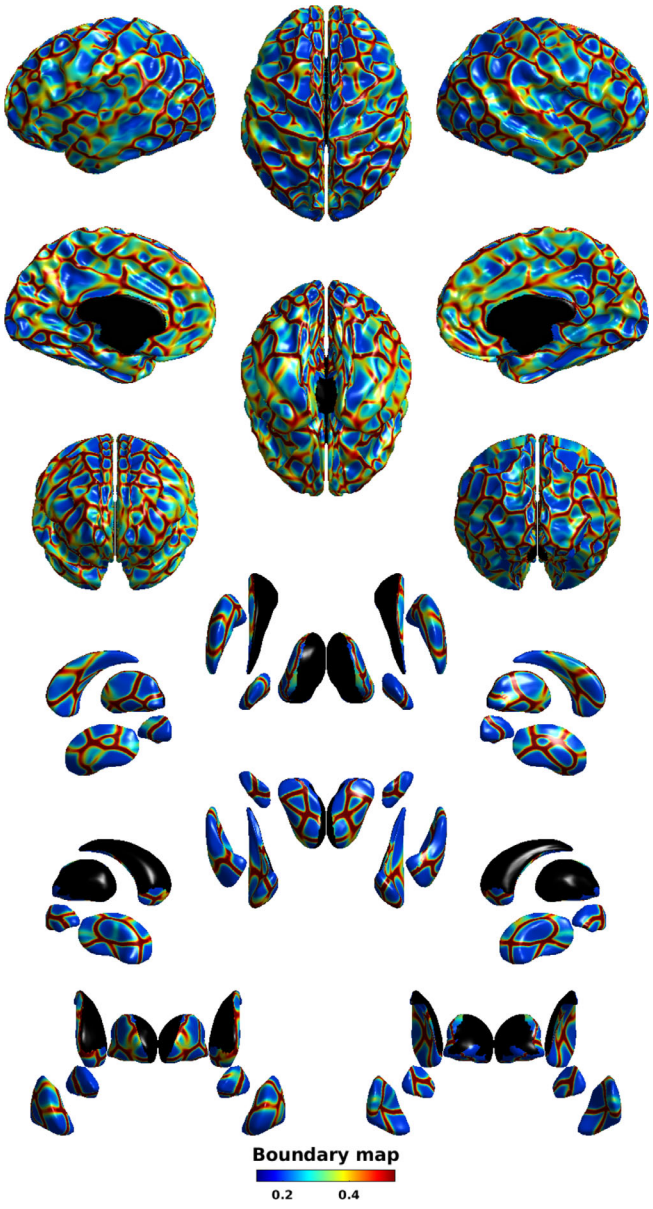

FIGURE 2 The connectivity-based boundary map. The top half of the figure shows the cortical results; the bottom half shows the subcortical results, with the same set of orientations as the cortical results. Note that the spatial aspect of the subcortical structures has been manipulated to reveal the map of each structure in each orientation; but the position of each structure is nonetheless approximately correct. Notice that the watershed boundaries are generally quite clear

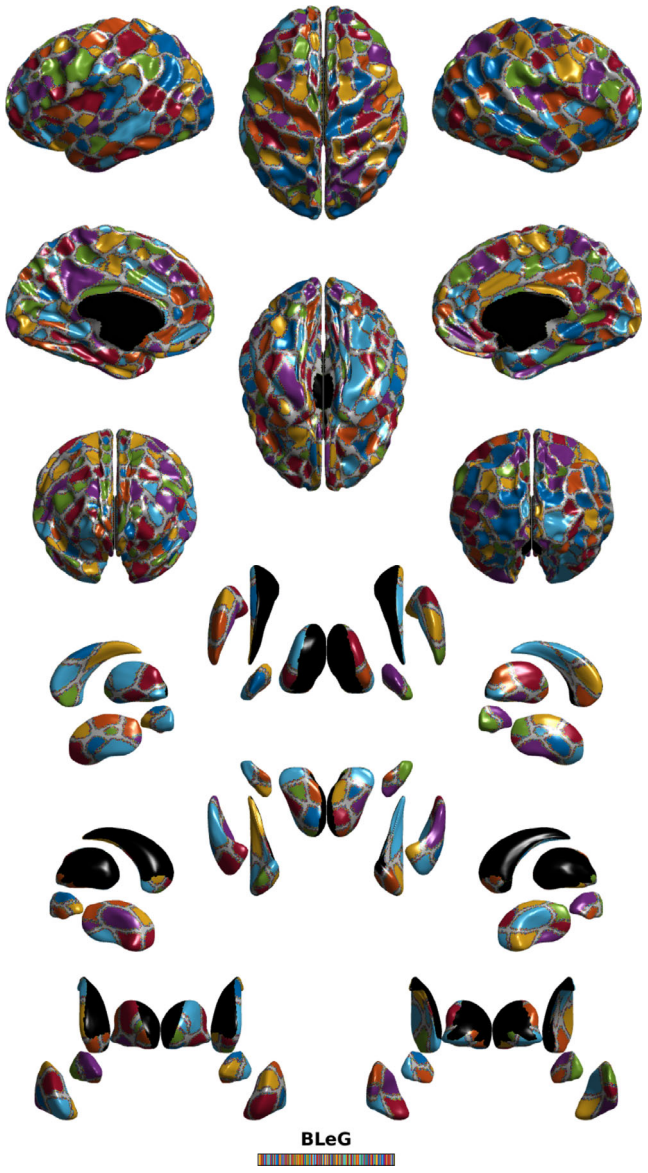

FIGURE 3 The connectivity-based BLeG parcellation. The top half of the figure shows the cortical results; the bottom half shows the subcortical results, with the same set of orientations as the cortical results. Note that the spatial aspect of the subcortical structures has been manipulated to reveal the map of each structure in each orientation; but the position of each structure is nonetheless approximately correct. Notice that the watershed boundaries in Figure 2 translate directly to the parcel boundaries

+ subcortical surface-based parcellation, we assess it in terms of the within-parcel homogeneity of the complexity of the models required to bestfit white/gray contrast measures (Lewis et al., 2018, 2019). We use white/gray contrast measures because they span both the cortical and the subcortical structures and because they are sensitive to age, sex, and brain size. We determine the linear models that best fit the data at each vertex, and the complexity of those models, and then assess the within-parcel homogeneity of model complexity. The mean of this parcel-wise homogeneity of model complexity provides a measure of how well the overall connectivity-based parcellation aligns with the age-, sex-, and brain size-related differences in white/gray contrast measures. Both the functional and structural assessments of within-parcel homogeneity are done for the BLeG parcellation in comparison to parcellations based on arbitrary divisions of the surface meshes but with the same number of parcels and same mean parcel size as the BLeG parcellation.

2.3.1 | Assessment of within-parcel functional homogeneity

For each parcellation, we determined the parcel-wise homogeneity of the fMRI connectivity patterns. We define the homogeneity of fMRI connectivity for a parcel *p* to be the mean of the correlations between the connectivity patterns of all pairs of vertices within parcel *p*, across subjects. We define the within-parcel homogeneity of fMRI connectivity for the overall parcellation as the mean of the homogeneity of all parcels.

We assess the within-parcel homogeneity of fMRI connectivity for our BLeG parcellation and for parcellations based on arbitrary divisions of the surface meshes. We generated 100 parcellations with random parcels. These were generated by seeding random vertices in each structure, and then iteratively (a) growing parcels out from each seed until they collided with another parcel, and (b) discarding the smallest parcel once further expansion was not possible; this process continued until the number of parcels matched that of the BLeG parcellation for each structure. Thus, these were random parcellations in terms of the placement of the parcels, but each random parcellation had the same number of parcels in each structure as does the BLeG parcellation, and was constructed such that the mean size of the parcels did not differ significantly from the BLeG parcellation. This is shown in Figure S2. We then compute the median of the mean within-parcel homogeneity of fMRI connectivity across the 100 random parcellations, the median absolute deviation of the within-parcel homogeneity across all random parcellations, and the improvement in the within-parcel homogeneity of the BLeG parcellation relative to the median for these random parcellations, in terms of median absolute deviations from the median of the random parcellations.

2.3.2 | Comparison of BLeG parcels to known anatomy

Gordon et al. (2016) demonstrated that these methods produce a parcellation that, at least for the cortex, aligns reasonably well with known cytoarchitectonic areas, particularly primary visual, motor, and sensory cortices. They visually compared their cortical parcels to the probabilistic borders of these cortical areas, as mapped by Van Essen et al. (2012) based on cytoarchitectonic maps produced by Fischl et al. (2008). We repeat this analysis, but instead of probabilistic maps for these areas, we rely on the mapping provided by Glasser, Coalson, et al. (2016). In addition, we extend this approach to the subcortical structures, but in this case, we rely on schematic descriptions of the anatomy of the structures. A consensus description is available only for the thalamus; we compare our BLeG parcellation of the thalamus to that.

2.3.3 | Assessment of parcellation stability across the life-span

Additionally, we assessed the stability of the parcellation across the life-span by creating parcellations for the data of individuals between 6 and 18 years of life and for the data of individuals between 70 and 85 years of life, and comparing both of them to the BLeG parcellation, constructed from the data of individuals between 19 and 69 years of life. These parcellations were compared via their Dice coefficients. This tests the sensitivity of the method to age-related differences in connectivity, both during development and senescence, and also the applicability of our BLeG parcellation for use with data outside of the age-range of the data from which it was created.

2.3.4 | Assessment of BLeG with white/gray contrast

Finally, and most relevant to the main point of producing this cortical and subcortical surface-based parcellation, we assess our BLeG parcellation in terms of its usefulness with surface-based measures; specifically, we demonstrate this for white–gray contrast measures (Lewis et al., 2018, 2019). To generate the white/gray contrast measures, two additional surfaces were created from each of the surfaces at the gray–white boundary: a sub-white surface below the gray–white boundary, that is, inside the white matter, and a supra-white surface above the gray–white boundary, that is, inside the gray matter. The T1-weighted intensities were then read onto these surfaces, and at each vertex, the value on the sub-white surface was divided by the value on the supra-white surface. For the cortex, the sub-white surface was placed 1 mm beneath the surface at the inner edge of the cortical gray matter and the supra-white surface was placed 35% of the way from the surface at the gray-white boundary to the surface at the gray-CSF boundary. For the subcortical structures, because of the lesser spatial constraints, the sub-white surfaces were placed 2 mm outside of the surfaces at the gray–white boundaries, and the supra-white surfaces were placed 2 mm inside of the surfaces at the gray–white boundaries. These surfaces are shown in Figure 4. To create the surfaces on either side of the gray–white boundary, a distance map was created from the surfaces at the gray–white boundary (both cortical and subcortical), smoothed with a Gaussian kernel, and used to create a gradient vector field. The cortical white surface was moved 1 mm inward along this gradient vector field to produce a sub-white surface, and outward 35% of the distance to the gray surface to produce a supra-white surface. The same procedure produced the contrast measures for the subcortical surfaces, but moving inward and outward 2 mm. This procedure ensures that the sub-white surfaces in regions with thin strands of white matter will not cross, and so will provide the best possible approximation of white matter. This can be seen in Figure 4 between subcortical structures and within thin gyri. Notice, however, that areas of the sub-white surfaces of the caudate and thalamus fall within the ventricles rather than white matter, and thus the white/gray contrast measures in these areas will not be valid and must be masked. This is, of course, also the case for the brainstem and midsagittal cuts.

The intensity values on the T1-weighted image were sampled at each vertex of both the supra-white surfaces and the sub-white surfaces, and the ratio was formed by dividing the value at each vertex of

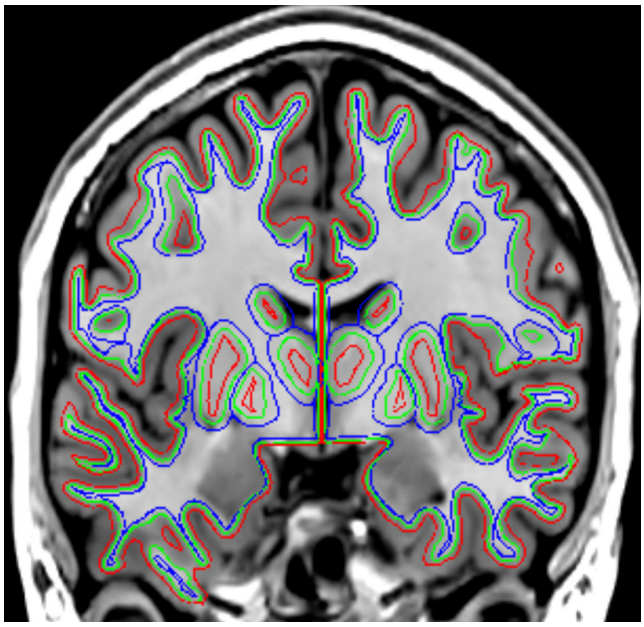

FIGURE 4 An example of the surfaces used to form the white/gray contrast measures. The surface at the gray–white boundary is shown in green. Copies of these surfaces were moved into gray matter (red) and white matter (blue) along with the gradient vectors of a distance map based on the surface at the gray–white boundary. Gray matter and white matter intensity were then measured at each of the vertices of these derivative surfaces, and the white/gray contrast measure formed as the ratio of white intensity to gray intensity at corresponding vertices of the two surfaces. Note that in areas with thin strands of white matter sub-white surfaces about rather than cross. Note also that areas of the sub-white surface of the caudate and thalamus fall in the ventricles; measures in these areas are invalid and must be masked

the sub-white surface by the value at the corresponding vertex of the supra-white surface. The intensity values were sampled in stereotaxic space, with the T1-weighted volume upsampled to 0.5 mm iso, with no non-uniformity correction or normalization. This avoids, to the extent possible, issues arising from differences in brain size, while leaving the intensity values essentially unchanged.

At each vertex, we determined the best-fit model to the contrast data from all models comprised of terms including any of "AGE," "SEX," and "BRAINVOL" (total), as well as any of the composite terms "AGE^2," "AGE^3," and the interaction terms for any of "SEX," "BRAINVOL," and "AGE^{1-3}." The best-fit model was determined by searching all possible models and choosing the one with the lowest value for the Akaike information criterion (AIC; Akaike, 1976). Each model was evaluated using the SurfStat toolbox.[4] We then determined the complexity of the best-fit model at each vertex. We defined *model complexity* (*mc*) as the sum of the number of terms, with composite terms counted as the number of base terms in the composite term raised to the power 0.5, capturing the intuition that, for example, "1 + AGE + AGE^{2}" ($mc = 3.4142$) should be more complex than "1 + AGE + SEX" ($mc = 3$), but less complex than "1 + AGE + SEX + BRAINVOL" ($mc = 4$). This yielded the map in Figure S3.

For each parcellation, we determined the parcel-wise homogeneity of model complexity, and compared the homogeneity of model complexity for our BLeG parcellation to the homogeneity of model complexity for the arbitrary divisions of the surface meshes described in Section 2.3.1. We define the homogeneity of model complexity for a parcel p to be $1/(1 + std[mc_p])$, where mc_p is the vector comprised of the model complexity at each vertex within parcel p. Thus, the homogeneity of model complexity for a parcel ranges from 0 to 1, with greater variation in the model complexity at each vertex within the parcel yielding lower homogeneity of model complexity for the parcel. We define the homogeneity of model complexity of the overall parcellation as the mean of the parcel-wise homogeneity of model complexity. We assess the homogeneity of model complexity for our BLeG parcellation and for the 100 random parcellations; we then compute the median and median absolute deviation of the homogeneity of model complexity across the 100 random parcellations, and the relation of the BLeG parcellation to these random parcellations in terms of median absolute deviations from the median of the random parcellations.

3 | RESULTS

3.1 | Assessment of BLeG with fMRI connectivity patterns

The results of the test of the homogeneity of within-parcel fMRI connectivity-based patterns for the BLeG parcellation are shown in Figure 5. The BLeG parcellation shows mean within-parcel fMRI connectivity homogeneity significantly greater than the median of random parcellations with the same number of parcels and a mean parcel size that is not different from the BLeG parcellation. As shown in Figure 5, this greater mean within-parcel fMRI homogeneity is present in the cortex as well as in each of the subcortical structures. Thus, the BLeG parcellation captures the patterns of functional connectivity to a far greater extent than would be expected from the size of the parcels alone, and this is true for parcels throughout the cortex and the subcortical structures.

Moreover, as shown in Figures S5 and S6, this is also the case for data other than that from which the BLeG parcellation was created, including, for example, children, adolescents, and the elderly.

3.2 | Comparison of BLeG parcels to known anatomy

The comparison of our BLeG parcellation to the pictorial description of the consensus anatomy of the thalamus is shown in Figure 6. Our BLeG parcellation excludes the portion of the thalamus adjacent to the ventricles, which is approximately the region medial to the internal medullary lamina, and so the comparison applies only to the lateral nuclei. This comparison yields a good correspondence. The consensus anatomy shows eight subnuclei internal to the thalamus; each of these

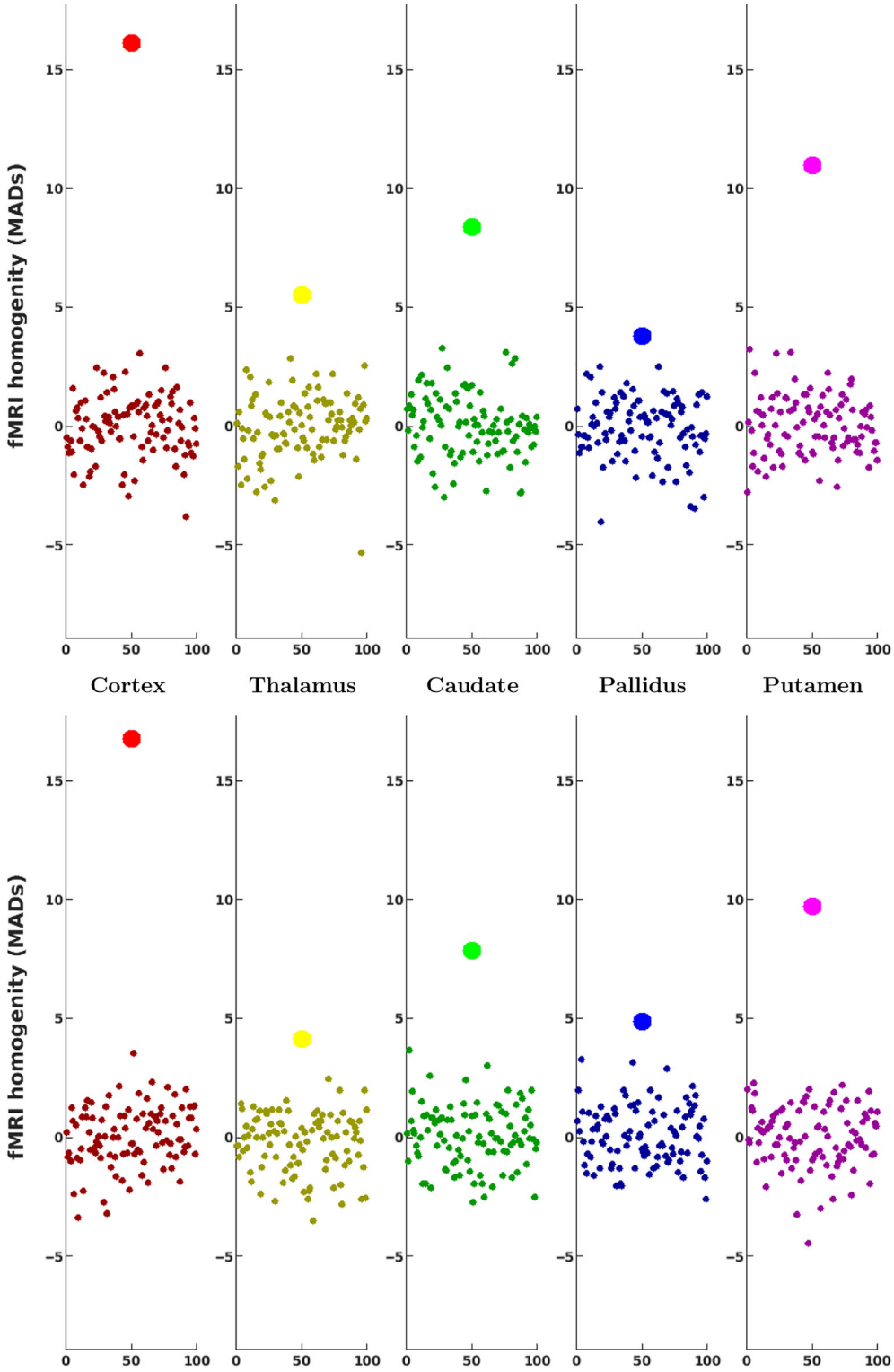

FIGURE 5 Mean within-parcel fMRI connectivity homogeneity for the BLeG parcellation compared to for random parcellations. The mean within-parcel fMRI connectivity homogeneities for the BLeG parcellation (large dots) are greater than those for random parcellations (small dots) for all structures. Note that the comparison for the cortex is shown in red; the comparison for the thalamus in yellow; that for the caudate in green; that for the globus pallidus in blue; and the comparison for the putamen is shown in magenta. The comparisons of the left hemisphere structures are shown on the top row; the comparison for the right hemisphere structures is shown on the bottom row. The *y*-axis is the mean within-parcel fMRI connectivity homogeneity for each parcellation, centered on the median across all parcellations, and measured in median absolute deviations from that median. The *x*-axis is the index of each of the 100 parcellations

can be directly mapped to the thalamic BLeG parcels. However, it should be noted that the *anterior nuclear group* comprises the anteromedial, anterodorsal, and anteroventral nuclei (Morel, Magnin, & Jeanmonod, 1997); and since we mask out the medial nuclei, we see here only the anterodorsal, and anteroventral nuclei. Further, it should be kept in mind that the consensus anatomy is provided as a schematic, and so only approximates the positions of the nuclei via notions of anterior or posterior, medial or lateral, and dorsal or ventral, and is not intended to accurately convey the shape of the nuclei, or the boundaries between them. Note also that the lateral and medial geniculate nuclei are not represented in the BLeG parcellation, since the fMRI data were sampled 2 mm inside the surface of the thalamus, and so not inside these very small structures that protrude from the thalamus.

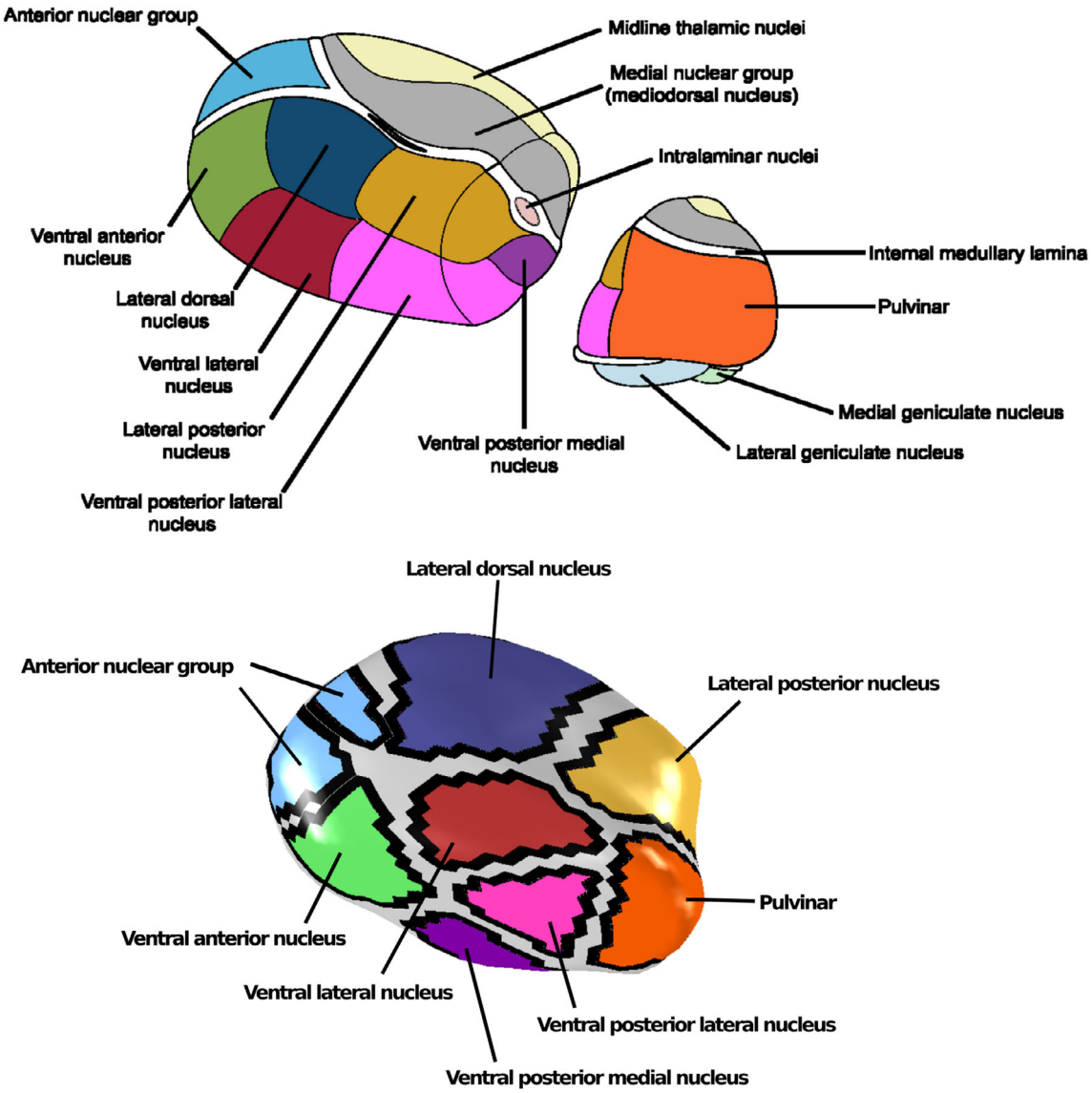

FIGURE 6 Comparison of the BLeG parcellation of the thalamus to the pictorial description of its consensus anatomy [Illustration provided by Moises Dominguez, MD and Lineage Medical, LLC]. Note that the pictorial description of the thalamus is viewed from above and via a cross-sectional cut to show the midline thalamic nuclei and the medial nuclear group as well as the ventral posterior medial nucleus, whereas our BLeG parcellation masks out the portion of the thalamus adjacent to the ventricles, essentially discarding the areas medial to the internal medullary lamina, and so is shown in a fully lateral view. Comparing the BLeG parcellation to the consensus anatomy for the portion of the thalamus lateral to the internal medullary lamina shows a one-to-one correspondence, with the anterior nuclear group further divided into its anterodorsal and anteroventral subparts. However, it should be noted that a perfect correspondence should not be expected; the pictorial description is a schematic, and so only approximates the positions of the nuclei via notions of anterior or posterior, medial or lateral, and dorsal or ventral. Note also that the fMRI data are measured 2 mm inside the thalamic surface, and so activity in, for example, the lateral and medial geniculate nuclei is not measured

The comparison of our BLeG parcellation to the cortical anatomy considered the motor and sensory cortices, and the primary and secondary visual cortices. Primary visual cortex is essentially Brodmann area 17, which is the pericalcarine cortex; secondary visual cortex is Brodmann area 18, which is a narrow band of cortex surrounding area V1; primary motor cortex is standardly thought to be contained within the pre-central gyrus; and primary sensory cortex within the post-central gyrus. The boundaries of these areas are taken from the multi-modal parcellation of Glasser, Coalson, et al. (2016) as mapped to the CIVET-2.1.0 surfaces using multimodal surface matching (MSM) surface registration (Lewis et al., 2020). Those regions are shown in Figure 7 together with the BLeG parcels that overlap each region.

The excellent agreement of the BLeG parcellation with the boundaries of the calcarine fissure suggests that, at least for V1, the BLeG parcellation well-captures the anatomical structure of cortex. In the cases of the primary motor and sensory cortices, this is less clear. The anatomically defined divisions of the pre- and post-central gyri do not show the same solid agreement with the BLeG parcellation. The

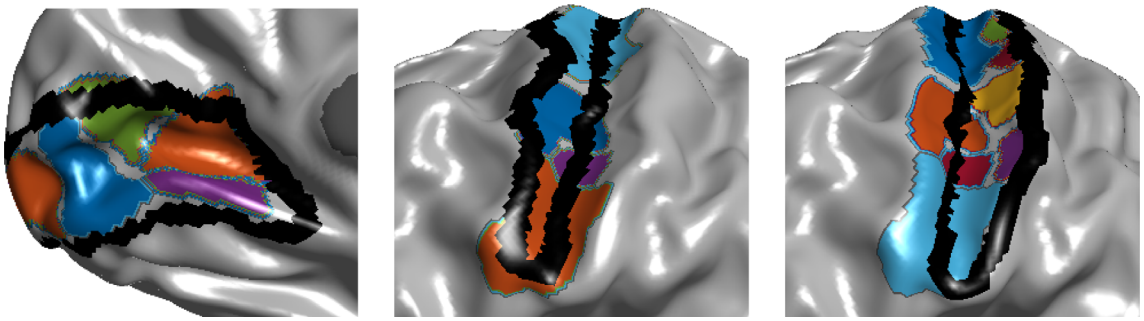

FIGURE 7 BLeG parcels compared to cortical anatomy. The left subfigure shows the boundary of the left V1 (black line) and the BLeG parcels within it. Notice that there are multiple parcels within the boundary, and that none of them extends substantially beyond the boundary. The middle subfigure shows the parcels within the boundaries of Brodmann area 4 (shown in black), that is, M1, and the BLeG parcels within it. Notice that these parcels largely fall within the boundary of area 4, but often extend beyond the nadir of the central sulcus. The right subfigure shows the boundary of Brodmann area 3 (shown in black), that is, S1, and the BLeG parcels within it. Notice the overlap of the parcels in M1 and S1

BLeG parcels often extend across the nadir of the central sulcus, and sulci in general; rather the gyral crowns seem to separate regions showing differences in functional connectivity patterns.

3.3 | Assessment of parcellation stability across the life-span

The watershed boundaries computed for the individuals between 6 and 18 years of age and for those between 70 and 85 years of age are shown in Figure S4. Notice that the two appear to be quite similar, and both appear to be similar to the BLeG boundary map shown in Figure 2. It should be noted that the boundary map for individuals less than 19 years of age is constructed from data from only 115 individuals, and the boundary map for the individuals between 70 and 85 years of age is constructed from only 60 individuals. Nonetheless, the resulting parcellations are similar for all three. The Dice coefficient for the comparison of the adult BLeG to the developmental BLeG is 0.868; the Dice coefficient for the comparison of the adult BLeG to the elderly BLeG is 0.822.

Further evidence of the validity of our BLeG parcellation for data from across the life-span is provided in Figures S5 and S6. These figures show the assessment of within-parcel fMRI-connectivity homogeneity in the developmental data and in the data from the elderly.

3.4 | Assessment of BLeG with white/gray contrast

The results of the test of the use of our BLeG parcellation with the model complexity of the surface-based measures of white/gray contrast are shown in Figure 8. The BLeG parcellation generally shows greater mean within-parcel model complexity homogeneity than do the random parcellations with the same number of parcels in each structure and a mean parcel size that is not different from the BLeG parcellation. However, interestingly, this is less true for the cortex than for any of the subcortical structures. The bilateral thalamus, caudate, and putamen all show mean within-parcel model complexity homogeneity that is several median absolute deviations greater for the BLeG parcellation than for the random parcellations; while the bilateral globus pallidus, the smallest structure, shows mean within-parcel model complexity homogeneity only slightly greater than that of the random parcellations. Thus, the BLeG parcellation captures the patterns of model complexity within the white/gray contrast data to a far greater extent than would be expected from the size of the parcels alone, but this is true to a lesser extent for the cortex than for the subcortical structures.

4 | DISCUSSION

Drawing on our recent work using label-based fusion methods to identify the thalamus, caudate, putamen, and globus pallidus, which we then fitted surfaces to; we extended Gordon et al.'s (2016) surface-based rs-fMRI connectivity parcellation approach to include also these deep gray-matter structures. We generated a functional parcellation of both the cortical and subcortical surfaces using the portion of the life-span data from the Enhanced Nathan Klein Institute—Rockland Sample (Nooner et al., 2012) comprised of data from 393 individuals between 19 and 69 years of age. We call this the Bezgin–Lewis extended Gordon (BLeG) parcellation, and we provide it for the use of the neuroimaging community.[5]

The cortical portion of our BLeG parcellation is surprisingly dissimilar to Gordon et al.'s parcellation; the methods are, for the most part, identical, other than the subcortical structures here being represented as surfaces rather than volumes. There are 392 cortical BLeG regions (left 194; right 198). The Gordon parcellation has 356 parcels (178 in either hemisphere), though 422 parcels before the elimination of parcels deemed to be unreliable. In addition to these differences, a direct comparison of the two parcellations yields a Dice coefficient of only 0.62. However, these discrepancies might stem from a number of sources. First, there are substantial differences in the resolution of

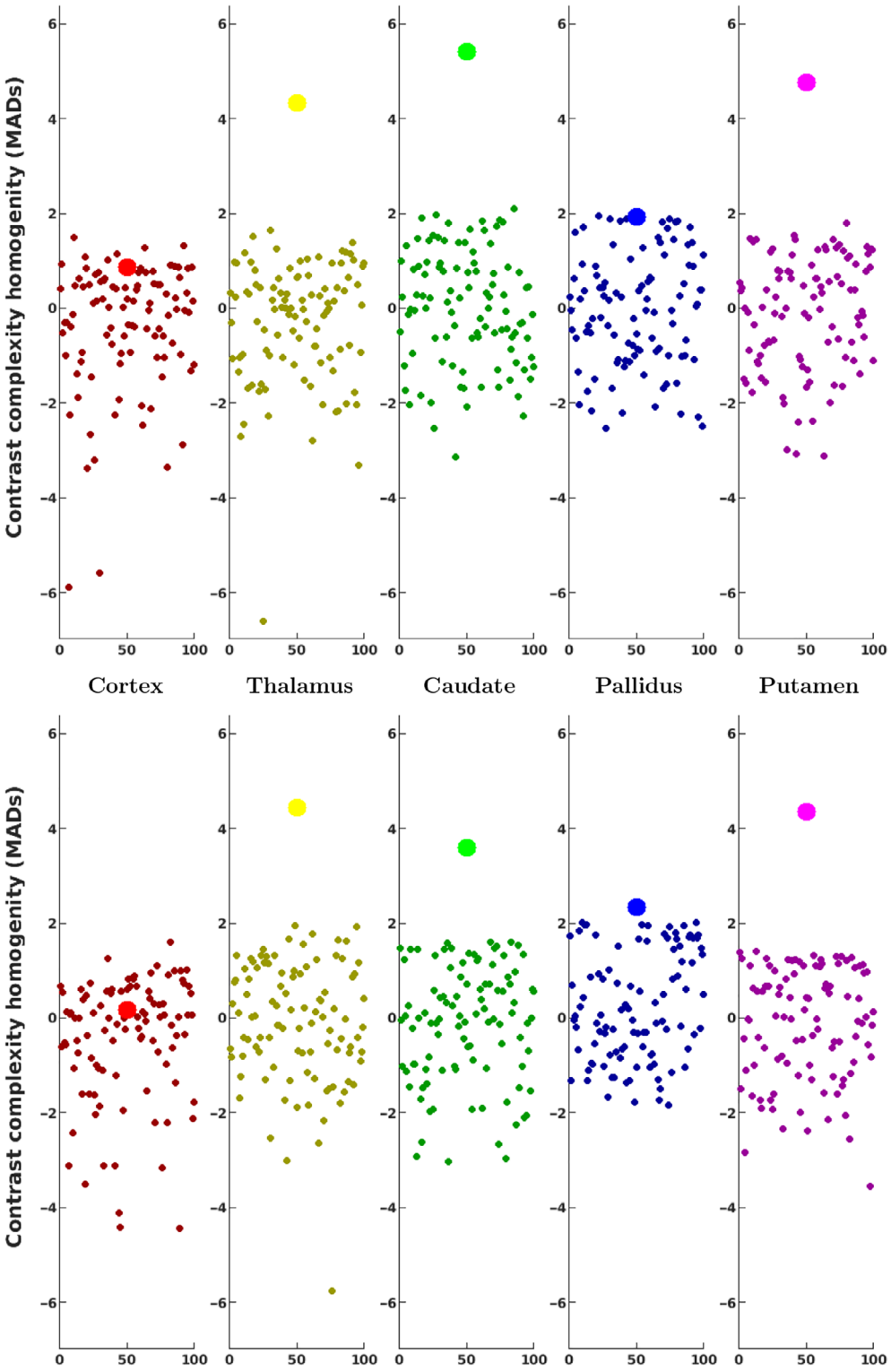

FIGURE 8 Median within-parcel white/gray contrast model complexity homogeneity for the BLeG parcellation compared to for random parcellations. The median within-parcel white/gray contrast model complexity homogeneities for the BLeG parcellation (large dots) are generally greater than those for random parcellations (small dots). Note that the comparison for the cortex is shown in red; the comparison for the thalamus in yellow; that for the caudate in green; that for the globus pallidus in blue; and the comparison for the putamen is shown in magenta. The comparisons of the left hemisphere structures are shown on the top row; the comparison for the right hemisphere structures is shown on the bottom row. The *y*-axis is the median within-parcel white/gray contrast model complexity for each parcellation, centered on the median across all parcellations, and measured in median absolute deviations from that median. The *x*-axis is the index of each of the 100 parcellations

the data: the Gordon et al. (2016) data have a spatial resolution of $4 \times 4 \times 4$ mm, and a temporal resolution of 2.5 s; the NKI-RS samples have a spatial resolution of $2 \times 2 \times 2$ mm, and a temporal resolution of 1.4 s. It is unclear to exactly what extent those differences should impact the parcellation. The higher spatial resolution of the NKI-RS data used for our BLeG parcellation compared to the data used by Gordon et al. (2016) most likely eliminates substantial noise from partial volume effects, which may be a cause of the low-SNR parcels, and may provide a sort-of blurring. The results of our parcellation with the low-resolution data indicate that this is indeed the case. The parcellation based on the low-resolution data has far fewer parcels, and comparison with the Gordon et al. (2016) parcellation yields an improved Dice coefficient of 0.66. However, this is still far from a perfect agreement between the two parcellations. However, the data

used by Gordon et al. were lower resolution still. Also, our sample size was substantially larger than that used by Gordon et al., that is, 393 versus 120; and the age-range of the data used by Gordon et al. was 19–32 years of age, whereas we used that portion of the NKI-RS data with subjects between 19 and 69 years of age. Functional connectivity patterns are known to be similar across the life-span, but there are some age-related differences (Han et al., 2018). Further investigation is needed to determine to what extent each of these differences accounts for the differences between the Gordon et al. (2016) parcellation and our BLeG parcellation. On the other hand, the similarities across the BLeG parcellation and its developmental and elderly counterparts suggest that the sample differences do not play a major role, and the only slight improvement in Dice similarity for the low-resolution versus high-resolution parcellation in comparison to the Gordon et al. (2016) parcellation suggests that the resolution of the data has only a modest effect on the outcome; so the implication is that scanner and protocol differences play a major role in producing these parcellation differences.

As per Gordon et al. (2016), we looked at the alignment of our parcellation with regions of the brain with more or less consensus architectures. For the cortex, we looked at the primary visual, motor, and sensory cortices. In the Gordon et al. parcellation, the primary visual cortex contained a single parcel; in our BLeG parcellation, it contained multiple parcels, but with those parcels, for the most part, respecting the borders of V1. The primary motor cortex, that is, Brodmann area 4, comprised multiple parcels for both the Gordon et al. parcellation and our BLeG parcellation, but with more parcels in the Gordon et al. parcellation. These parcels seem to roughly respect the boundaries of M1, though less so toward the gyral crown in the Gordon et al. parcellation, and more so toward the nadir of the central sulcus. This is also the case for the primary sensory cortex, that is, Brodmann areas 3a and 3b, but in this case, the extension of the parcels across the nadir of the central sulcus is more pronounced in our BLeG parcellation. The source of this difference between our BLeG parcellation and the Gordon et al. parcellation is unclear; perhaps there are differences in the accuracy of the placement of the surfaces within the sulci. But it is worth noting that Brodmann area 3a, which lies at the nadir of the central sulcus, is considered an area of sensorimotor integration, responsible for proprioception, and is thus not truly distinct from either motor functions or more truly purely sensory functions. In the case of the subcortical structures, there was consensus architecture only for the thalamus. As shown in Figure 6, our BLeG parcellation of the thalamus is in good agreement with the schematic description of the consensus anatomy, allowing that the anterior nuclear group can divide into its dorsal and ventral parts.

A more thorough assessment of our BLeG parcellation of the subcortical structures would be preferable, but consensus architecture is lacking for structures other than the thalamus, and even for the thalamus, it is only schematic. Nonetheless, there are points of apparent disagreement that are worth consideration. The globus pallidus, for instance, appears to comprise two anatomical structures: the globus pallidus internal and external. Our BLeG parcellation instead divides the globus pallidus into four regions on the left, and three on the right. Recent work suggests that the globus pallidus, in fact, divides into three regions: the external segment, the lateral internal segment, and the medial internal segment (Kita, 2010). However, there is no evidence to support either an asymmetry, or a division of the globus pallidus into four parcels. Nonetheless, this parcellation yields increased fMRI homogeneity compared to random parcellations with the same number of parcels and the same mean parcel size, and increased homogeneity of model complexity compared to random parcellations.

As a part of their verification of their parcellation, Gordon et al. used a second dataset to show that the method produced similar boundary maps in both datasets. Their verification dataset was acquired with a similar protocol, and had a similar age-range to that from which their parcellation was constructed; and the boundary maps for the two were, indeed, similar. We, again, followed Gordon et al., but with a major difference: we divided the full NKI-RS dataset into those less than 19 years of age, those 70 years of age or greater, and those 19–69 years of age. The BLeG parcellation was constructed from the individuals between 19 and 69 years of age; the other two sets of individuals provided verification datasets. However, note that, whereas the verification dataset used by Gordon et al. simply showed that the method replicated the parcellation, our verification additionally shows that the method replicates the parcellation in children and adolescents, as well as in the elderly. The comparison of the BLeG parcellation and the parcellation from children and adolescents yielded a Dice coefficient of 0.868; the comparison of the BLeG parcellation and the parcellation from individuals over 70 years of age yielded a Dice coefficient of 0.822. Further, we assessed within-parcel fMRI connectivity homogeneity also in these two verification datasets, as well as our BLeG parcellation; all three parcellations showed an increase relative to the within-parcel fMRI connectivity homogeneity based on random parcels with the same number of parcels and mean parcel size for each structure, and that increase was similar across all three parcellations. These results seem adequate to support the suggestion that our BLeG parcellation is suitable for use with subjects from childhood to senescence. Although, as noted by Han et al. (2018), differences between parcellations based on samples from different time periods across the life-span preclude direct comparisons, the three parcellations nonetheless show far more similarities than differences. Our BLeG parcellation is arguably a good parcellation to use to allow results from different samples with different age ranges to be compared.

Finally, we assessed the use of our BLeG parcellation with white/gray contrast metrics from the NKI-RS life-span data, that is, all of the data from 6 to 85 years of age. We computed the best-fit model to the contrast data at each vertex, and then measured the within parcel homogeneity of the complexity of these models for both our BLeG parcellation and random parcellations with the same number of parcels and same mean parcel size as the BLeG parcellation in each structure. The results showed a general increase in within-parcel model complexity homogeneity across structures, but with the cortex showing the least increase. It is interesting to contrast this with the fact that the cortex showed the greatest increase in within-parcel

homogeneity with fMRI connectivity patterns. However, the lower within-parcel homogeneity of model complexity may be because the cortex shows little variation in model complexity compared to the subcortical structures. In any case, the generally increased within-parcel homogeneity of model complexity in the BLeG parcellation compared to in random parcellations with the same number of parcels and same mean parcel size as the BLeG parcellation in each structure argues for the utility of our BLeG parcellation with surface-based measures that span the cortex and the subcortical structures.

In summary, building on Gordon et al.'s (2016) surface-based rs-fMRI connectivity parcellation approach, and on Lewis et al.'s (2019) methods for labeling and putting surfaces on the subcortical material, we have extended Gordon et al.'s method to include the deep structures as well as the cortex. We have applied this extended methodology to data from the Enhanced Nathan Klein Institute—Rockland Sample (Nooner et al., 2012), limited to the data from individuals from 19 to 69 years of age, and generated the Bezgin–Lewis extended Gordon (BLeG) parcellation. We have shown that our BLeG parcellation has much higher within-parcel rs-fMRI connectivity homogeneity than should be expected based on parcel size alone (Figure 5). We have shown that the parcels of the BLeG parcellation correspond reasonably well with the known anatomy of both cortical and subcortical areas (Figures 6 and 7). We have shown that the BLeG parcellation compares well with the parcellation built from the data from children and adolescents, and also with the parcellation built from the data from the elderly (Figure S4). We have shown that within-parcel fMRI connectivity homogeneity with the BLeG parcellation is increased in all age groups relative to that seen with random parcellations with the same number of parcels and same mean parcel size as the BLeG parcellation (Figures 5, S5, and S6). And we have shown that within-parcel model complexity homogeneity for gray/white contrast is higher for the BLeG parcellation than should be expected based on parcel size alone (Figure 8), thus providing some evidence that this extension of the Gordon et al. parcellation to include the subcortical structures is suitable for use with surface-based measures of both the cortex and the subcortical structures.

However, some caveats should be noted. First, we have not performed global signal regression. Truly global noise has been shown to have no impact on parcellation (Glasser et al., 2018; Glasser, Coalson, et al., 2016), but methods such as global signal regression remove signal and negatively impact parcellation boundaries (Glasser et al., 2018). Second, our modification to ICA-AROMA to preserve ICA components with high-frequency content that appear unrelated to motion is non-standard, and should receive a more careful verification. Third, though there are certainly gains made by using a surface-based approach in terms of registration (Anticevic et al., 2008; Fischl et al., 2008; Klein et al., 2010; Lyttelton et al., 2007), there are also potential losses. Whereas the cortex is fairly indisputably, at least at the resolution of fMRI, a 2D structure, that is less clear for the deep gray matter. There is a potentially important third dimension to the deep gray-matter structures. The intralaminar nuclei of the thalamus, for instance, are potentially lost in a surface-based analysis. This could, of course, be dealt with by generating surfaces at multiple depths within the deep gray-matter structures; but we have not done this here. There are also deep gray-matter structures that are difficult to fit surfaces to, for example, the hippocampus; and we have not. Likewise, the cerebellum has such fine structure in terms of gray-matter folds that it is exceedingly difficult to perform tissue segmentation on and to fit surfaces to; and we have not. It should also be noted that though surface registration overcomes many of the problems that volumetric registration suffers from, it is also flawed. The gyrification-related information that drives surface registration can leave ambiguities that lead to misregistration of the surfaces. Thus, the surface data must be verified. Moreover, though surface registration generally properly aligns the data of matching sulci and gyri, there is little information to force alignment along the length of a gyrus or sulcus. An approach that utilizes multi-modal data, for example, that of Glasser, Coalson, et al. (2016), may yield superior results. In addition, it is worth noting that the approach used here to extend Gordon et al.'s surface-based approach to parcellation to include the subcortical structures is in no way specific to Gordon et al.'s approach; our extension could easily be adapted to other surface-based approaches.

However, we believe that we have demonstrated the worth of incorporating the subcortical structures into a surface-based parcellation, for the benefits it provides for registration of these structures, for the benefits it provides in terms of a uniform representation of the cortex and the subcortical structures, and as a means of achieving dimensionality reduction that is based in a biological reality. We provide our BLeG parcellation for the use of the neuroimaging community with the hope that it proves useful.

ACKNOWLEDGMENTS

This research has been supported by grant ANRP-MIRI13-3388 from the Azrieli Neurodevelopmental Research Program in partnership with the Brain Canada Multi-Investigator Research Initiative (to Alan C. Evans), and by grants from the Canadian Institutes of Health Research (to Alan C. Evans and to D. Louis Collins), and grants from the Natural Sciences and Engineering Research Council of Canada (to D. Louis Collins). It also benefited from computational resources provided by Compute Canada (www.computecanada.ca) and Calcul Quebec (www.calculquebec.ca). Finally, we thank Lindsay Lewis for providing the Glasser, Coalson, et al. (2016) multi-modal parcellation on the CIVET-2.1.0 surfaces. And we thank her and Andrew Reid for help with creating the FreeSurfer and GIFTI representations that we provide in the public release.

CONFLICT OF INTEREST

The authors declare no conflicts of interest.

DATA AVAILABILITY STATEMENT

The Bezgin-Lewis-extended-Gordon parcellation together with the surfaces for the cortex and the subcortical structures are available on G-Node at https://gin.g-node.org/johndlewis/BLeG. The NKI-RS data are publicly available at http://fcon_1000.projects.nitrc.org/indi/enhanced/. CIVET-2.1.0 is available at https://github.com/aces/CIVET_Full_Project. The label-fusion-based labeling code is available

at https://github.com/vfonov/nist_mni_pipelines. The code to create the fMRI surfaces is available at https://github.com/vfonov/cortex_walk. The code for the surface-based parcellation is available at https://sites.wustl.edu/petersenschlaggarlab/gordon2016surface_parcellation_distribute-20agwt4/.

ORCID

John D. Lewis https://orcid.org/0000-0002-0832-7396
Gleb Bezgin https://orcid.org/0000-0002-1069-9201
Vladimir S. Fonov https://orcid.org/0000-0003-3402-7749
D. Louis Collins https://orcid.org/0000-0002-8432-7021
Alan C. Evans https://orcid.org/0000-0003-3841-6098

ENDNOTES

[1] https://github.com/aces/CIVET_Full_Project.

[2] https://sites.wustl.edu/petersenschlaggarlab/gordon2016surface_parcellation_distribute-20agwt4/.

[3] https://www.nitrc.org/projects/cifti/.

[4] SurfStat is available at http://www.math.mcgill.ca/keith/surfstat/.

[5] https://gin.g-node.org/johndlewis/BLeG.

REFERENCES

Akaike, H. (1976). An information criteron (AIC). *The Mathematical Scientist*, *14*, 5–7.

Aljabar, P., Heckemann, R. A., Hammers, A., Hajnal, J. V., & Rueckert, D. (2009). Multi-atlas based segmentation of brain images: Atlas selection and its effect on accuracy. *NeuroImage*, *46*, 726–738.

Allen, J. S., Bruss, J., Brown, C. K., & Damasio, H. (2005). Normal neuroanatomical variation due to age: The major lobes and a parcellation of the temporal region. *Neurobiology of Aging*, *26*, 1245–1260.

Amunts, K., Kedo, O., Kindler, M., Pieperhoff, P., Mohlberg, H., Shah, N., … Zilles, K. (2005). Cytoarchitectonic mapping of the human amygdala, hippocampal region and entorhinal cortex: Intersubject variability and probability maps. *Anatomy and Embryology*, *210*, 343–352.

Anticevic, A., Dierker, D. L., Gillespie, S. K., Repovs, G., Csernansky, J. G., Van Essen, D. C., & Barch, D. M. (2008). Comparing surface-based and volume-based analyses of functional neuroimaging data in patients with schizophrenia. *NeuroImage*, *41*, 835–848.

Beucher, S.. (1979). Use of watersheds in contour detection. In: *Proceedings of the International Workshop on Image Processing (CCETT)*.

Brodmann, K. (1909). *Vergleichende Lokalisationslehre der Grosshirnrinde in ihren Prinzipien dargestellt auf Grund des Zellenbaues*. Leipzig: Barth.

Coalson, T. S., Van Essen, D. C., & Glasser, M. F. (2018). The impact of traditional neuroimaging methods on the spatial localization of cortical areas. *Proceedings of the National Academy of Sciences of the United States of America*, *115*, E6356–E6365.

Cohen, A. L., Fair, D. A., Dosenbach, N. U., Miezin, F. M., Dierker, D., Van Essen, D. C., … Petersen, S. E. (2008). Defining functional areas in individual human brains using resting functional connectivity MRI. *NeuroImage*, *41*, 45–57.

Collins, D. L., Neelin, P., Peters, T. M., & Evans, A. C. (1994). Automatic 3D intersubject registration of MR volumetric data in standardized Talairach space. *Journal of Computer Assisted Tomography*, *18*, 192–205.

Collins, D. L., & Pruessner, J. C. (2010). Towards accurate, automatic segmentation of the hippocampus and amygdala from MRI by augmenting ANIMAL with a template library and label fusion. *NeuroImage*, *52*, 1355–1366.

Coupé, P., Manjón, J. V., Fonov, V., Pruessner, J., Robles, M., & Collins, D. L. (2011). Patch-based segmentation using expert priors: Application to hippocampus and ventricle segmentation. *NeuroImage*, *54*, 940–954.

Edelman, R. R., Siewert, B., Darby, D. G., Thangaraj, V., Nobre, A. C., Mesulam, M. M., & Warach, S. (1994). Qualitative mapping of cerebral blood flow and functional localization with echo-planar MR imaging and signal targeting with alternating radio frequency. *Radiology*, *192*, 513–520.

Esteban, O., Markiewicz, C. J., Blair, R. W., Moodie, C. A., Isik, A. I., Erramuzpe, A., … Gorgolewski, K. J. (2019). Fmriprep: A robust preprocessing pipeline for functional MRI. *Nature Methods*, *16*, 111–116.

Fischl, B., Rajendran, N., Busa, E., Augustinack, J., Hinds, O., Yeo, B. T., … Zilles, K. (2008). Cortical folding patterns and predicting cytoarchitecture. *Cerebral Cortex*, *18*(8), 1973–1980.

Fischl, B., Sereno, M. I., Tootell, R. B., & Dale, A. M. (1999). High-resolution intersubject averaging and a coordinate system for the cortical surface. *Human Brain Mapping*, *8*, 272–284.

Frost, M. A., & Goebel, R. (2012). Measuring structural–functional correspondence: Spatial variability of specialised brain regions after macro-anatomical alignment. *NeuroImage*, *59*, 1369–1381.

Glasser, M. F., Coalson, T. S., Bijsterbosch, J. D., Harrison, S. J., Harms, M. P., Anticevic, A., … Smith, S. M. (2018). Using temporal ICA to selectively remove global noise while preserving global signal in functional MRI data. *NeuroImage*, *181*, 692–717.

Glasser, M. F., Coalson, T. S., Robinson, E. C., Hacker, C. D., Harwell, J., Yacoub, E., … Van Essen, D. C. (2016). A multi-modal parcellation of human cerebral cortex. *Nature*, *536*, 171–178.

Glasser, M. F., Smith, S. M., Marcus, D. S., Andersson, J. L., Auerbach, E. J., Behrens, T. E., … Van Essen, D. C. (2016). The human connectome project's neuroimaging approach. *Nature Neuroscience*, *19*, 1175–1187.

Goddings, A. L., Mills, K. L., Clasen, L. S., Giedd, J. N., Viner, R. M., & Blakemore, S. J. (2014). The influence of puberty on subcortical brain development. *NeuroImage*, *88*, 242–251.

Goldstein, J. M., Seidman, L. J., Horton, N. J., Makris, N., Kennedy, D. N., Caviness, V. S., Jr., … Tsuang, M. T. (2001). Normal sexual dimorphism of the adult human brain assessed by in vivo magnetic resonance imaging. *Cerebral Cortex*, *11*, 490–497.

Gordon, E. M., Laumann, T. O., Adeyemo, B., Huckins, J. F., Kelley, W. M., & Petersen, S. E. (2016). Generation and evaluation of a cortical area parcellation from resting-state correlations. *Cerebral Cortex*, *26*, 288–303.

Greve, D. N., & Fischl, B. (2018). False positive rates in surface-based anatomical analysis. *NeuroImage*, *171*, 6–14.

Han, L., Savalia, N. K., Chan, M. Y., Agres, P. F., Nair, A. S., & Wig, G. S. (2018). Functional parcellation of the cerebral cortex across the human adult lifespan. *Cerebral Cortex*, *28*, 4403–4423.

Heckemann, R. A., Hajnal, J. V., Aljabar, P., Rueckert, D., & Hammers, A. (2006). Automatic anatomical brain MRI segmentation combining label propagation and decision fusion. *NeuroImage*, *33*, 115–126.

Hirai, T., & Jones, E. (1989). A new parcellation of the human thalamus on the basis of histochemical staining. *Brain Research Reviews*, *14*, 1–34.

Hu, X., Le, T. H., Parrish, T., & Erhard, P. (1995). Retrospective estimation and correction of physiological fluctuation in functional MRI. *Magnetic Resonance in Medicine*, *34*, 201–212.

Jenkinson, M., Bannister, P., Brady, M., & Smith, S. (2002). Improved optimization for the robust and accurate linear registration and motion correction of brain images. *NeuroImage*, *17*, 825–841.

Kennedy, K. M., Erickson, K. I., Rodrigue, K. M., Voss, M. W., Colcombe, S. J., Kramer, A. F., … Raz, N. (2009). Age-related differences in regional brain volumes: A comparison of optimized voxel-based morphometry to manual volumetry. *Neurobiology of Aging*, *30*, 1657–1676.

Kim, J. S., Singh, V., Lee, J. K., Lerch, J., Ad-Dab'bagh, Y., MacDonald, D., … Evans, A. C. (2005). Automated 3-D extraction and evaluation of the inner and outer cortical surfaces using a Laplacian map and partial volume effect classification. *NeuroImage*, *27*, 210–221.

Kim, S. G. (1995). Quantification of relative cerebral blood flow change by flow-sensitive alternating inversion recovery (fair) technique: Application to functional mapping. *Magnetic Resonance in Medicine*, *34*, 293–301.

Kita, H. (2010). Organization of the globus pallidus. In H. Steiner & K. Y. Tseng (Eds.), *Handbook of Behavioral Neuroscience* (Vol. 20, pp. 233–247). Amsterdam: Elsevier.

Klein, A., Ghosh, S. S., Avants, B., Yeo, B. T., Fischl, B., Ardekani, B., … Parsey, R. V. (2010). Evaluation of volume-based and surface-based brain image registration methods. *NeuroImage*, *51*, 214–220.

Klein, J. C., Behrens, T. E., Robson, M. D., Mackay, C. E., Higham, D. J., & Johansen-Berg, H. (2007). Connectivity-based parcellation of human cortex using diffusion MRI: Establishing reproducibility, validity and observer independence in BA 44/45 and SMA/pre-SMA. *NeuroImage*, *34*, 204–211.

Lewis, J. D., Evans, A. C., Tohka, J., & The Brain Development Cooperative Group. (2018). T1 white/gray contrast as a predictor of chronological age, and an index of cognitive performance. *NeuroImage*, *173*, 341–350.

Lewis, J. D., Fonov, V. S., Collins, D. L., Evans, A. C., Tohka, J., & The Brain Development Cooperative Group. (2019). Cortical and subcortical T1 white/gray contrast, chronological age, and cognitive performance. *NeuroImage*, *196*, 276–288.

Lewis, L. B., Lepage, C. Y., Glasser, M. F., Coalson, T. S., Van Essen, D. C., & Evans, A. C., 2020. A multimodal surface matching (MSM) surface registration pipeline to bridge atlases across the MNI and the FreeSurfer/Human Connectome Project worlds. In: *26th Annual Meeting of the Organization for Human Brain Mapping (OHBM 2020)*, p. 100.

Lötjönen, J. M., Wolz, R., Koikkalainen, J. R., Thurfjell, L., Waldemar, G., Soininen, H., … Alzheimer's Disease Neuroimaging Initiative. (2010). Fast and robust multi-atlas segmentation of brain magnetic resonance images. *NeuroImage*, *49*, 2352–2365.

Lyttelton, O., Boucher, M., Robbins, S., & Evans, A. (2007). An unbiased iterative group registration template for cortical surface analysis. *NeuroImage*, *34*, 1535–1544.

Manjón, J. V., Coupé, P., Martí-Bonmatí, L., Collins, D. L., & Robles, M. (2010). Adaptive non-local means denoising of MR images with spatially varying noise levels. *Journal of Magnetic Resonance Imaging*, *31*, 192–203.

Mayer, A. R., Ling, J. M., Dodd, A. B., Shaff, N. A., Wertz, C. J., & Hanlon, F. M. (2019). A comparison of denoising pipelines in high temporal resolution task-based functional magnetic resonance imaging data. *Human Brain Mapping*, *40*, 3843–3859.

Miller, M. I., Beg, M. F., Ceritoglu, C., & Stark, C. (2005). Increasing the power of functional maps of the medial temporal lobe by using large deformation diffeomorphic metric mapping. *Proceedings of the National Academy of Sciences of the United States of America*, *102*, 9685–9690.

Morel, A., Magnin, M., & Jeanmonod, D. (1997). Multiarchitectonic and stereotactic atlas of the human thalamus. *Journal of Comparative Neurology*, *387*, 588–630.

Nooner, K. B., Colcombe, S., Tobe, R., Mennes, M., Benedict, M., Moreno, A., … Milham, M. P. (2012). The NKI-Rockland sample: A model for accelerating the pace of discovery science in psychiatry. *Frontiers in Neuroscience*, *6*, 152.

Østby, Y., Tamnes, C. K., Fjell, A. M., Westlye, L. T., Due-Tønnessen, P., & Walhovd, K. B. (2009). Heterogeneity in subcortical brain development: A structural magnetic resonance imaging study of brain maturation from 8 to 30 years. *Journal of Neuroscience*, *29*, 11772–11782.

Pipitone, J., Park, M. T. M., Winterburn, J., Lett, T. A., Lerch, J. P., Pruessner, J. C., … Alzheimer's Disease Neuroimaging Initiative. (2014). Multi-atlas segmentation of the whole hippocampus and subfields using multiple automatically generated templates. *NeuroImage*, *101*, 494–512.

Power, J. D., Barnes, K. A., Snyder, A. Z., Schlaggar, B. L., & Petersen, S. E. (2012). Spurious but systematic correlations in functional connectivity MRI networks arise from subject motion. *NeuroImage*, *59*, 2142–2154.

Pruim, R. H., Mennes, M., van Rooij, D., Llera, A., Buitelaar, J. K., & Beckmann, C. F. (2015). ICA-aroma: A robust ICA-based strategy for removing motion artifacts from fMRI data. *NeuroImage*, *112*, 267–277.

Raz, N., Gunning, F. M., Head, D., Dupuis, J. H., McQuain, J., Briggs, S. D., … Acker, J. D. (1997). Selective aging of the human cerebral cortex observed in vivo: Differential vulnerability of the prefrontal gray matter. *Cerebral Cortex*, *7*, 268–282.

Raz, N., Lindenberger, U., Rodrigue, K. M., Kennedy, K. M., Head, D., Williamson, A., … Acker, J. D. (2005). Regional brain changes in aging healthy adults: General trends, individual differences and modifiers. *Cerebral Cortex*, *15*, 1676–1689.

Raz, N., & Rodrigue, K. M. (2006). Differential aging of the brain: Patterns, cognitive correlates and modifiers. *Neuroscience & Biobehavioral Reviews*, *30*, 730–748.

Salat, D. H., Lee, S. Y., van der Kouwe, A., Greve, D. N., Fischl, B., & Rosas, H. D. (2009). Age-associated alterations in cortical gray and white matter signal intensity and gray to white matter contrast. *NeuroImage*, *48*, 21–28.

Sled, J. G., Zijdenbos, A. P., & Evans, A. C. (1998). A nonparametric method for automatic correction of intensity nonuniformity in MRI data. *IEEE Transactions on Medical Imaging*, *17*, 87–97.

Smith, S. M., Jenkinson, M., Woolrich, M. W., Beckmann, C. F., Behrens, T. E., Johansen-Berg, H., et al. (2004). Advances in functional and structural MR image analysis and implementation as FSL. *NeuroImage*, *23*, S208–S219.

Sowell, E. R., Peterson, B. S., Kan, E., Woods, R. P., Yoshii, J., Bansal, R., … Toga, A. W. (2006). Sex differences in cortical thickness mapped in 176 healthy individuals between 7 and 87 years of age. *Cerebral Cortex*, *17*, 1550–1560.

Storsve, A. B., Fjell, A. M., Tamnes, C. K., Westlye, L. T., Overbye, K., Aasland, H. W., & Walhovd, K. B. (2014). Differential longitudinal changes in cortical thickness, surface area and volume across the adult life span: Regions of accelerating and decelerating change. *Journal of Neuroscience*, *34*, 8488–8498.

Tohka, J., Zijdenbos, A., & Evans, A. (2004). Fast and robust parameter estimation for statistical partial volume models in brain MRI. *NeuroImage*, *23*, 84–97.

Tucholka, A., Fritsch, V., Poline, J. B., & Thirion, B. (2012). An empirical comparison of surface-based and volume-based group studies in neuroimaging. *NeuroImage*, *63*, 1443–1453.

Turner, R., & Geyer, S. (2014). Comparing like with like: The power of knowing where you are. *Brain Connectivity*, *4*, 547–557.

Tzourio-Mazoyer, N., Landeau, B., Papathanassiou, D., Crivello, F., Etard, O., Delcroix, N., … Joliot, M. (2002). Automated anatomical labeling of activations in SPM using a macroscopic anatomical parcellation of the MNI MRI single-subject brain. *NeuroImage*, *15*, 273–289.

Van Essen, D. C., Glasser, M. F., Dierker, D. L., Harwell, J., & Coalson, T. (2012). Parcellations and hemispheric asymmetries of human cerebral cortex analyzed on surface-based atlases. *Cerebral Cortex*, *22*, 2241–2262.

Weier, K., Fonov, V., Lavoie, K., Doyon, J., & Collins, D. L. (2014). Rapid automatic segmentation of the human cerebellum and its lobules (RASCAL)—Implementation and application of the patch-based label-fusion technique with a template library to segment the human cerebellum. *Human Brain Mapping*, *35*, 5026–5039.

Wig, G. S., Laumann, T. O., Cohen, A. L., Power, J. D., Nelson, S. M., Glasser, M. F., … Petersen, S. E. (2013). Parcellating an individual subject's cortical and subcortical brain structures using snowball sampling of resting-state correlations. *Cerebral Cortex*, *24*, 2036–2054.

Wig, G. S., Laumann, T. O., & Petersen, S. E. (2014). An approach for parcellating human cortical areas using resting-state correlations. *NeuroImage*, *93*, 276–291.

Zijdenbos, A. P., Forghani, R., & Evans, A. C. (2002). Automatic "pipeline" analysis of 3-D MRI data for clinical trials: application to multiple sclerosis. *IEEE Transactions on Medical Imaging*, *21*, 1280–1291.

Zilles, K., & Amunts, K. (2009). Receptor mapping: Architecture of the human cerebral cortex. *Current Opinion in Neurology*, *22*, 331–339.

Zilles, K., & Amunts, K. (2010). Centenary of Brodmann's map—Conception and fate. *Nature Reviews Neuroscience*, *11*, 139–145.

SUPPORTING INFORMATION

Additional supporting information may be found in the online version of the article at the publisher's website.

How to cite this article: Lewis, J. D., Bezgin, G., Fonov, V. S., Collins, D. L., & Evans, A. C. (2022). A sub+cortical fMRI-based surface parcellation. *Human Brain Mapping*, *43*(2), 616–632. https://doi.org/10.1002/hbm.25675